

# Efficient Vacuum-Deposited Perovskite Solar Cells with Stable Cubic $\text{FA}_{1-x}\text{MA}_x\text{PbI}_3$

Lidón Gil-Escrig, Chris Dreessen, Ismail Cihan Kaya, Beom-Soo Kim, Francisco Palazon, Michele Sessolo,\* and Henk J. Bolink



Cite This: *ACS Energy Lett.* 2020, 5, 3053–3061



Read Online

ACCESS |



Metrics & More

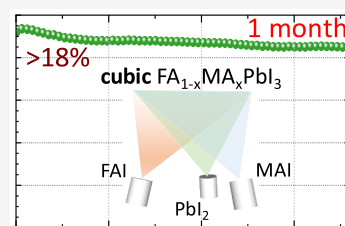


Article Recommendations



Supporting Information

**ABSTRACT:** Preparation of black formamidinium lead iodide (FAPbI<sub>3</sub>) requires high-temperature annealing and the incorporation of smaller A-site cations, such as methylammonium (MA<sup>+</sup>), cesium, or rubidium. A major advantage of vacuum processing is the possibility to deposit perovskite films at room temperature (RT), without any annealing step. Here we demonstrate stabilization of the cubic perovskite phase at RT, in a three-source co-sublimation method. We found that the MA<sup>+</sup> incorporation is a self-limiting process, where the amount of MA<sup>+</sup> which is incorporated in the perovskite is essentially unvaried with increasing MAI deposition rate. In this way a phase-pure, cubic perovskite with a bandgap of 1.53 eV can be obtained at room temperature. When used in fully vacuum-processed perovskite solar cells, PCEs up to 18.8% are obtained. Despite the presence of MA<sup>+</sup>, the solar cells were found to be thermally stable and maintained 90% of their initial efficiency after 1 month of continuous operation.



In a short period of time, solar cells based on organic–inorganic lead halide perovskites have rapidly advanced in terms of power conversion efficiency (PCE, now exceeding 25%), which is now comparable with more established thin-film and silicon solar cells.<sup>1–3</sup> Most of the reported high-efficiency perovskite solar cells use formamidinium (FA<sup>+</sup>) as the majority cation.<sup>4–6</sup> Compared to the archetypical methylammonium lead iodide (MAPbI<sub>3</sub>), formamidinium lead iodide (FAPbI<sub>3</sub>) displays a bandgap of 1.48 eV. According to the Shockley–Queisser limit, this is closer to the optimum bandgap value for a single-junction solar cell.<sup>7</sup> Moreover, FA<sup>+</sup> is more thermally stable than MA<sup>+</sup>, favoring the operational stability of the perovskite solar cells.<sup>8–11</sup> However, FAPbI<sub>3</sub> is characterized by a nonperovskite phase (“yellow” or  $\delta$ -FAPbI<sub>3</sub>) with wires of face-sharing PbI<sub>6</sub> octahedra, which is thermodynamically more stable than the desired cubic (“black” or  $\alpha$ -FAPbI<sub>3</sub>) perovskite phase at room temperature (RT). Preparation of  $\alpha$ -FAPbI<sub>3</sub> requires high-temperature annealing (typically above 150 °C), and the phase transition is reversible, meaning that in ambient atmosphere at RT the black FAPbI<sub>3</sub> converts back to the yellow phase.<sup>8,12</sup> Several studies have shown that replacing part of the FA<sup>+</sup> with MA<sup>+</sup> enables the stabilization of the cubic phase at RT, with improved photovoltaic performance.<sup>13–15</sup> This effect is attributed to the large dipole moment of the MA<sup>+</sup> cation, which leads to a stronger interaction with the lead halide octahedral cage and, therefore, a more stable crystal structure.<sup>16</sup> Recently, other cations such as cesium, rubidium, or guanidinium have also been incorporated into FAPbI<sub>3</sub> to improve its phase stability. Nonetheless, most of these

stabilizers widen the perovskite bandgap, reducing the attainable efficiency of the solar cells.<sup>12,17,18</sup> New compositions have been developed to maintain the bandgap of pure FAPbI<sub>3</sub>, in particular by incorporation of phenethylammonium lead iodide or by surface functionalization with other alkylammonium compounds;<sup>2,19</sup> however, the PCE is generally inferior compared with that of solar cells where FAPbI<sub>3</sub> is stabilized with MAI.<sup>20</sup>

The vast majority of these studies relied on solution-processed perovskite thin films. Vacuum deposition is an alternative method with important advantages over solution-processing, as it allows the deposition of pinhole-free, uniform, and smooth films.<sup>21–24</sup> Moreover, vacuum deposition gives a superior control over the film thickness and composition; it is compatible with large areas and eliminates the processing concerns related with the use of solvents.<sup>25–27</sup> To date, however, FA<sup>+</sup> has been scarcely employed in vacuum processing of perovskite films and solar cells. We and others have previously reported the fabrication of perovskite solar cells employing mixed cation (FA<sup>+</sup>, MA<sup>+</sup>, and Cs<sup>+</sup>) and mixed halide perovskites, a wide bandgap absorber suitable for tandem but not for single-junction solar cells.<sup>28,29</sup> The first example of narrow bandgap FAPbI<sub>3</sub> solar cells prepared by

Received: July 9, 2020

Accepted: August 26, 2020

Published: August 26, 2020



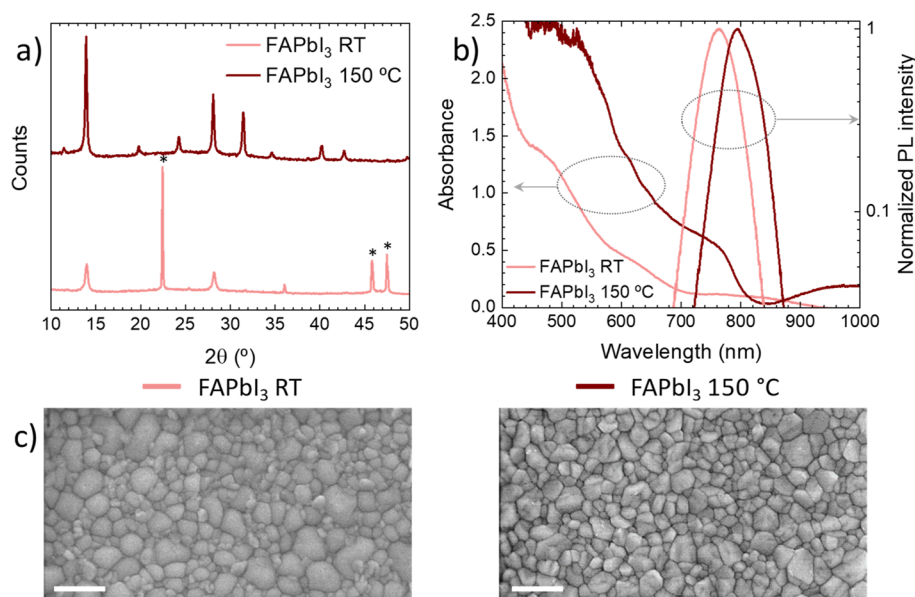


**Figure 1.** Characterization of as-deposited (RT) and annealed (150 °C) FAPbI<sub>3</sub> films. (a) XRD patterns where peaks marked with stars correspond to the yellow  $\delta$ -phase. (b) Absorption (left) and PL (right) spectra. (c) Comparison of the surface morphology by SEM (the scale bar corresponds to 500 nm).

vacuum methods was reported by Borchert et al.<sup>30</sup> The perovskite films were deposited by co-sublimation of FAI and PbI<sub>2</sub> in a high-vacuum chamber, followed by annealing at high temperature (170 °C) to form the black FAPbI<sub>3</sub> phase. They reported solar cells with average efficiency of 14% and record pixels up to 15.8%, albeit with significant hysteresis. No details regarding the film or device stability were reported. More recently, Chiang et al. described the deposition of perovskite films with nominal composition FA<sub>0.7</sub>Cs<sub>0.3</sub>Pb(I<sub>0.9</sub>Br<sub>0.1</sub>)<sub>3</sub>, obtained in a three-source deposition process using FAI, CsBr, and PbI<sub>2</sub>.<sup>31</sup> The corresponding solar cells (using spin-coated transport layers) showed very promising performance, with average efficiency of 16.8% and record pixels up to 18.2%. In order to obtain the black perovskite phase, they used an excess of FAI, and as a consequence, an annealing step at 135 °C was needed to crystallize the material. A major advantage of vacuum processing is the possibility to deposit perovskite films at room temperature, without any annealing step. This would make perovskite solar cells compatible with temperature-sensitive substrates (plastic foils and textiles) and allows their deposition on top of narrow bandgap absorbers in tandem architectures.<sup>32</sup>

In this study, we demonstrate the vacuum deposition of cubic perovskite films at RT. Stabilization of the perovskite phase is achieved through the addition of MAI, in a three-source co-sublimation method. We found that the MA<sup>+</sup> incorporation is a self-limiting process, where the amount of MA<sup>+</sup> incorporated in the perovskite is essentially unvaried with increasing MAI deposition rate. However, the deposition rate of MAI does have an influence on the phase-purity and film orientation. Interestingly, the perovskite with the smallest bandgap was obtained with the highest MAI deposition rate. In this way a phase-pure, cubic perovskite with a bandgap of 1.53 eV was obtained at room temperature. When used in fully vacuum-processed perovskite solar cells, PCEs up to 18.8% were obtained (18.6% on average). Moreover, the solar cells maintained 90% of their initial efficiency after 1 month of continuous operation.

Perovskite thin films were prepared in a vacuum chamber equipped with three thermal sources and integrated in a nitrogen-filled glovebox. In this way, exposure of the precursors and the deposited materials to the ambient atmosphere is prevented. Initially, we investigated the formation of FAPbI<sub>3</sub> by dual-source vacuum deposition of formamidinium iodide (FAI) and lead iodide (PbI<sub>2</sub>). The as-deposited films were analyzed by X-ray diffraction (XRD, Figure 1a and fit in Figure S1), which showed the coexistence of yellow ( $\delta$ ) and black ( $\alpha$ ) phases. In particular, intense peaks at  $2\theta = 22.5^\circ$ ,  $45.9^\circ$ , and  $47.5^\circ$  are observed, which correspond to the (002), (004), and (104) planes of  $\delta$ -FAPbI<sub>3</sub>.<sup>33</sup> This suggests a strong preferred orientation along the *c*-axis. It must be noted that the (001) and the (003) reflections, whose calculated positions should be around  $2\theta = 11.3^\circ$  and  $2\theta = 34.2^\circ$ , respectively, are systematically absent. This preferred orientation corresponds to the direction of the inorganic PbI<sub>6</sub> wires, meaning that they grow perpendicular to the substrate, in contrast to what is commonly observed for solution-processed films.<sup>34</sup> We noted also the presence of less intense diffraction signals corresponding to the  $\alpha$ -perovskite phase ( $2\theta = 14.0^\circ$  and  $28.2^\circ$ ). The optical characteristics of the films (Figure 1b), showing a weak absorption in the red part of the spectrum and a photoluminescence (PL) signal at 763 nm, are consistent with previous reports on the formation of a mixed  $\delta/\alpha$  (yellow/black) phase.<sup>35</sup> Figure 1a shows that after annealing at 150 °C for 10 min and cooling to RT, the yellow phase is mostly suppressed, and the diffractogram shows almost phase-pure  $\alpha$ -FAPbI<sub>3</sub>.<sup>36</sup> We note a small diffraction peak around  $2\theta = 11.6^\circ$ , ascribed to the (100) plane of  $\delta$ -FAPbI<sub>3</sub>, but its calculated intensity from Le Bail fits (Figure S2) is only 3.5% of the main  $\alpha$ -phase peak intensity. Also, as XRD measurements are carried out in air, it is possible that this weak contribution of  $\delta$ -FAPbI<sub>3</sub> is formed upon air exposure (degradation). In fact, the annealed black FAPbI<sub>3</sub> films turned into the yellow  $\delta$ -phase after 20–30 min in ambient conditions, as expected from previous reports.<sup>37</sup>

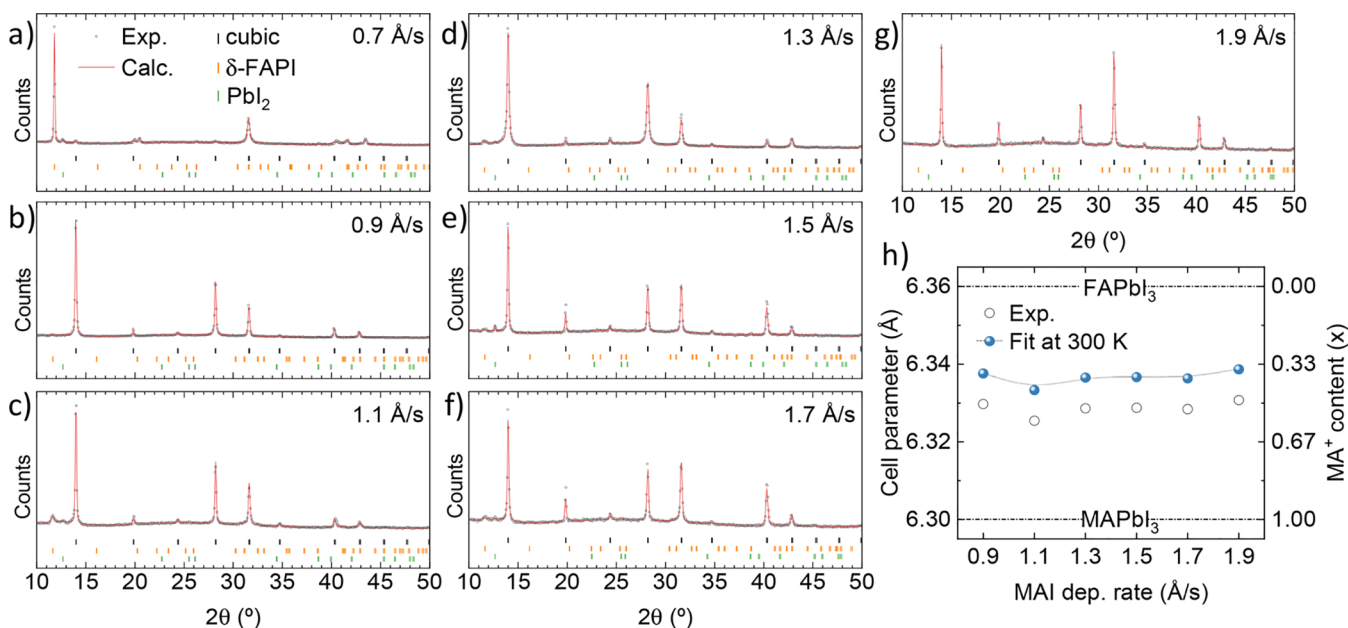


**Figure 2.** XRD characterization of FAMAPbI<sub>3</sub> films deposited with increasing MAI deposition rates. (a–g) Whole-pattern Le Bail fit (red line) of XRD patterns (open black circles). Vertical markers correspond to calculated Bragg's reflections for cubic  $\alpha$ -phase perovskite (black), yellow  $\delta$ -phase (yellow), and PbI<sub>2</sub> (green). (h) Unit cell parameter (left) as obtained from fit (open circles) and estimated values at 300 K, considering thermal expansion (solid spheres). On the right, the corresponding MA<sup>+</sup> content  $x$ , corresponding to the stoichiometry FA<sub>1-x</sub>MA<sub>x</sub>PbI<sub>3</sub>.

The black phase obtained after annealing is consistent with a cubic perovskite structure with  $Pm\bar{3}m$  space group and calculated lattice parameter of 6.346 Å. This lattice parameter is slightly smaller compared to the reported value for FAPbI<sub>3</sub> at 300 K (6.36 Å).<sup>38,39</sup> The discrepancy might be partly ascribed to thermal effects, as the temperature was not controlled during the XRD measurements. Considering the experimental temperature of 290 K and a linear thermal coefficient for the lattice parameter of  $7.9 \times 10^{-4} \text{ Å}\cdot\text{K}^{-1}$ ,<sup>38</sup> the corrected lattice parameter at 300 K would be 6.354 Å, which is very close to the reported value of 6.36 Å for  $\alpha$ -FAPbI<sub>3</sub>. Conversion to the desired black phase is also confirmed by the red-shifted absorption cut-off and PL emission (compared to that of the as-deposited phase), at approximately 800 nm, as expected for FAPbI<sub>3</sub>. The film morphology, as observed by scanning electron microscopy (SEM, Figure 1c), was found to be similar for the as-prepared and annealed films, with the latter showing a more faceted structure and narrower grain size distribution (diameter ranging from 100 to 300 nm). In order to test the optoelectronic properties of the FAPbI<sub>3</sub> films annealed at 150 °C, we fabricated fully vacuum-deposited p-i-n solar cells. Devices were prepared on indium tin oxide (ITO) coated glass slides, using molybdenum oxide (MoO<sub>3</sub>, 5 nm) and *N,N',N'',N''*-tetra([1,1'-biphenyl]-4-yl)-[1,1':4',1''-terphenyl]-4,4''-diamine (TaTm, 10 nm) as hole injection and transport layers (HIL and HTL), respectively. Then, a 500 nm thick perovskite film was deposited on TaTm and subsequently coated with fullerene (C<sub>60</sub>, 25 nm) and bathocuproine (BCP, 8 nm) as the electron transport and injection layers (ETL and EIL), respectively. The devices were completed with the deposition of a silver electrode (100 nm). Details of the device fabrication are reported in the Experimental Procedures. Figure S3a shows the external quantum efficiency (EQE) spectrum together with the integrated short-circuit current density ( $J_{sc}$ ) over the AM1.5

spectrum for a device obtained with FAPbI<sub>3</sub> annealed at 150 °C. The EQEs peaked at 90% and showed high values over the wavelength range 550–700 nm, with a lower response in the blue region (80% average EQE) and a drop close to the perovskite bandgap. The integrated  $J_{sc}$  was 21.3 mA cm<sup>-2</sup> and is in line with that obtained from current density versus voltage ( $J$ - $V$ ) curves under simulated 1 sun solar illumination (Figure S3b). The open-circuit voltage ( $V_{oc}$ ) and the fill factor (FF), however, were rather low (about 1 V and 60%, respectively), implying substantial nonradiative recombination and a large series resistance within the cells. The dark  $J$ - $V$  curves also showed a low shunt resistance, likely related to morphological or electronic defects within the perovskite or at the interface with transport layers.<sup>40</sup> Overall, the PCE was found to be about 11% on average with 13.0% for the best pixel, only slightly below the values previously reported for vacuum-processed FAPbI<sub>3</sub> solar cells.<sup>30</sup>

In the attempt to stabilize the perovskite cubic phase at RT, we added MAI from a third sublimation source during vacuum co-deposition. For the deposition of the FA<sub>1-x</sub>MA<sub>x</sub>PbI<sub>3</sub> (from now on called FAMAPbI<sub>3</sub> for simplicity) films, the individual quartz crystal microbalance (QCM) readings for FAI and PbI<sub>2</sub> were kept constant at deposition rates of 1 Å/s, while the deposition rate of MAI was varied between 0.7 and 1.9 Å/s. The XRD patterns for the entire series of vacuum-deposited perovskite films is displayed in Figure 2a–g, together with individual whole-pattern fits and reference Bragg's reflections (larger graphs are available in Figure S4). With the lowest MAI deposition rate (0.7 Å/s, Figure 2a), the film mainly consists of the yellow phase with the inorganic wires flat on the substrate, as evidenced by the main diffraction peak at  $2\theta = 11.7^\circ$  corresponding to the (100) plane of  $\delta$ -FAPbI<sub>3</sub> (space group  $P6_3/mcm$ ). As previously noted, this is also the main orientation observed for solution-processed films. It is, however, different than the as-deposited pure (MA-free)

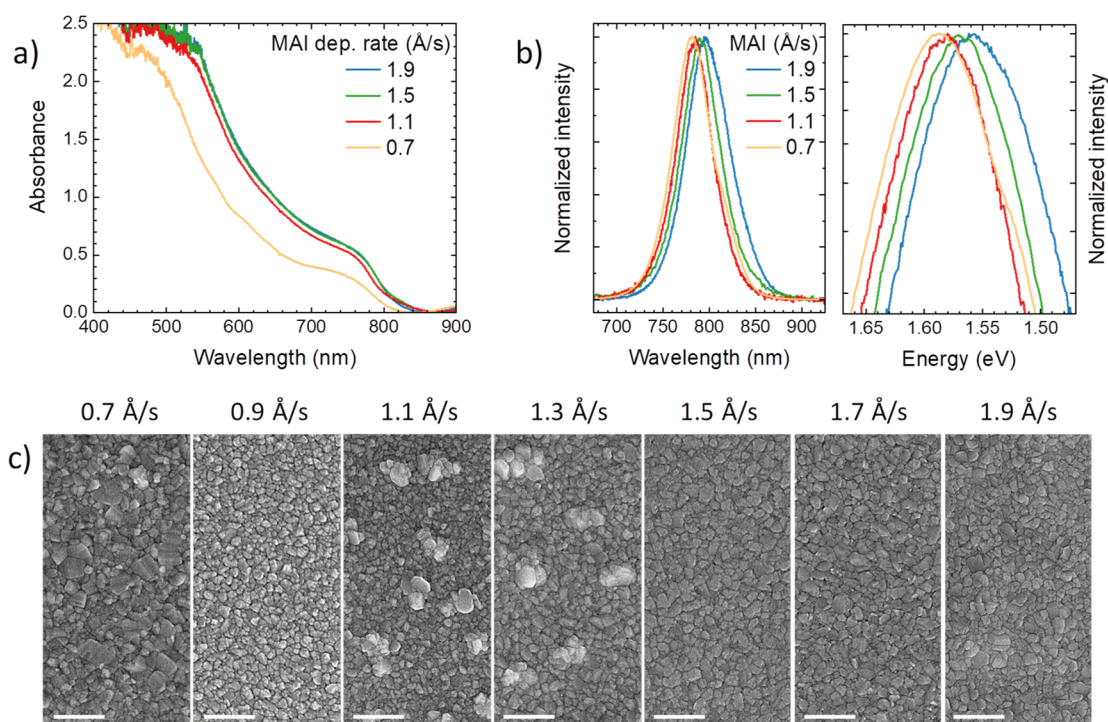


**Figure 3.** Optical properties and surface morphology for FAMAPbI<sub>3</sub> perovskite films obtained with increasing MAI deposition rates. (a) Optical absorption spectra. (b) PL spectra in linear (left) and semilogarithmic (right) scale with excitation at 520 nm. (c) Surface morphology as observed by SEM (scale bar 500 nm).

FAPbI<sub>3</sub> (Figure 1a). The reason for these different orientations is not clear, but it may originate from an increased disorder upon addition of MAI, something that, as will be discussed hereafter, also affects the  $\alpha$ -phase (at higher MAI rates). When the MAI deposition rate is increased from 0.9 to 1.9 Å/s, the film mainly consists of the cubic perovskite phase (Figure 2b–g). A close look at the  $2\theta = 11^\circ$ – $13.5^\circ$  range reveals the presence of the  $\delta$ -phase and of PbI<sub>2</sub> in some cases, but their relative signals are weak.

As a semiquantitative measure of phase purity, we plotted the ratio of the calculated intensity of the most intense  $\delta$ -phase and PbI<sub>2</sub> peaks with respect to the main  $\alpha$ -phase reflection in Figure S5. This shows that the impurities ( $\delta$ -phase and PbI<sub>2</sub>) are very low for all MAI rates greater than 0.7 Å/s, similar to the signal found on annealed FAPbI<sub>3</sub> (Figure 1a). At the highest MAI rate of 1.9 Å/s, no signal at all for the yellow phase or PbI<sub>2</sub> was found, and the perovskite film is essentially phase-pure. Also, we note again that the XRD is carried out in air, where conversion to the yellow phase is favored. The calculated lattice parameter for all samples is reported in Figure 2h. On average, we found a value of 6.33 Å, which is less than that obtained for pure FAPbI<sub>3</sub> (6.36 Å), but greater than that of cubic MAPbI<sub>3</sub> at 300 K (6.30 Å). This indicates that the smaller MA<sup>+</sup> cation is indeed incorporated in the lattice of the cubic perovskite, forming a mixed cation FA<sub>x</sub>MA<sub>1-x</sub>PbI<sub>3</sub> phase. The  $x$  value can be estimated by using the calibration curve from Weber et al.<sup>38</sup> Nevertheless, as noted previously in the discussion of Figure 1a, the values obtained herein should be corrected for thermal expansion. Applying the same correction as for pure FAPbI<sub>3</sub>, the lattice parameter of FA<sub>1-x</sub>MA<sub>x</sub>PbI<sub>3</sub> samples at 300 K increases to approximately 6.34 Å, which corresponds to the approximate stoichiometry FA<sub>0.6</sub>MA<sub>0.4</sub>PbI<sub>3</sub>. The fact that this stoichiometry does not seem to vary with MAI deposition rate is surprising and indicates that, within this

range, the incorporation of MA<sup>+</sup> in the lattice is self-limited and not directly related to its deposition rate. One of the benefits of vacuum deposition is the possibility to monitor the deposition rate of the different precursors in situ during the thin-film growth by quartz crystal microbalance (QCM) sensors. Even though this monitoring is not trivial in the case of MAI, with careful positioning of the QCMs we are able to determine the individual deposition rates. The monitored thickness by the QCM also suggests that the MAI incorporation does not increase after sublimation rates of 1.3 Å/s, resulting in the estimated  $x$  value in FA<sub>1-x</sub>MA<sub>x</sub>PbI<sub>3</sub> of 0.4–0.5, (Figure S6), in good agreement with the data obtained from the structural analysis. These results are in agreement with the nonstandard sublimation properties of MAI, whose adsorption on a surface is dependent on the temperature<sup>41</sup> as well as on the surface chemical composition.<sup>42</sup> The latter is of special importance for this work, as the temperature is kept constant at RT. For a given surface, in this case the forming FA<sub>1-x</sub>MA<sub>x</sub>PbI<sub>3</sub> film, increasing the deposition rate (as measured from a dedicated QCM in the vicinity of the thermal source) in a certain range does not lead to a proportionally higher MAI content in the film. This happens as there are not enough favorable adsorption sites for MAI on the surface of the film. It is worth noting that this is not true for FAI, as demonstrated in the Supporting Information. However, MAI seems to increase disorder in the films at high deposition rates (as seen by the progressive loss of orientation as observed by XRD), which might indicate the presence of amorphous MAI at the grain boundaries. The details of the procedure followed to quantify composition during vacuum co-sublimation are described in the Supporting Information.

Another interesting feature from the XRD signals of the FAMAPbI<sub>3</sub> series (with varying MAI deposition rates) is the difference in the relative intensities of the perovskite peaks,

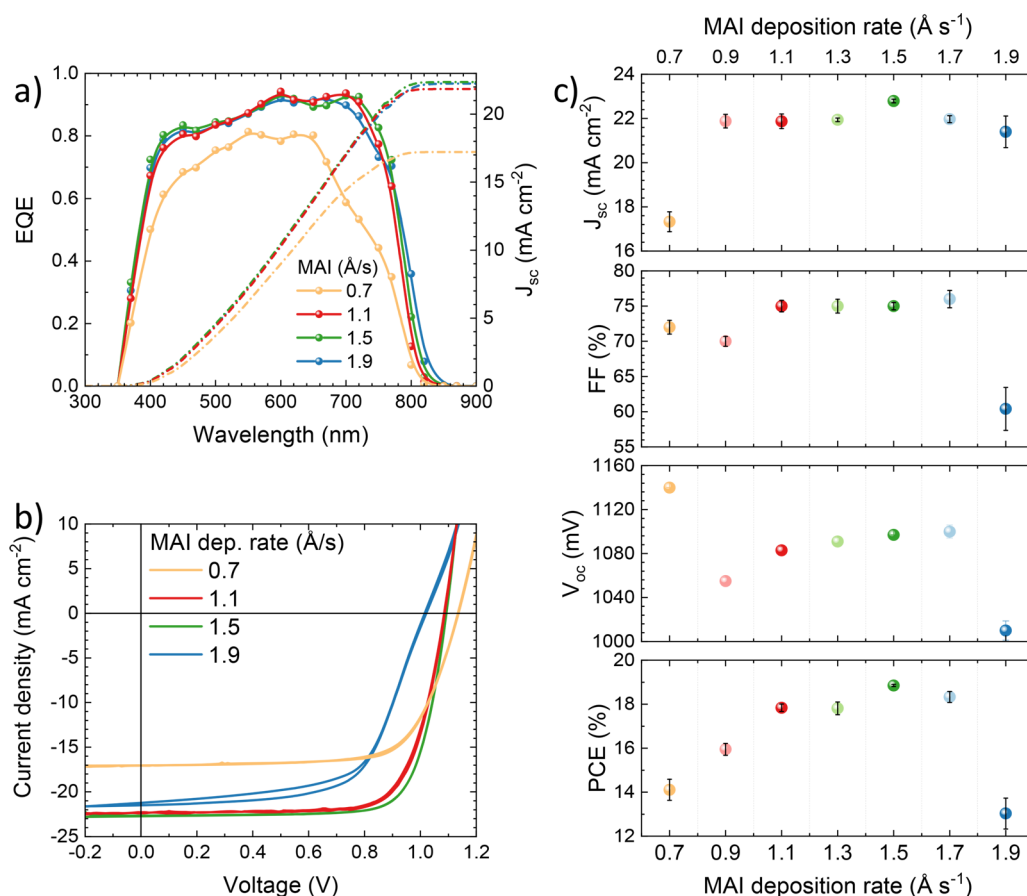


**Figure 4.** Characterization of perovskite solar cells with FAMAPbI<sub>3</sub> absorbers obtained with varying MAI deposition rates during vacuum processing. (a) External quantum efficiency (EQE) spectra. (b)  $J$ – $V$  curves under illumination for representative pixels and (c) summary of the average photovoltaic parameters for the all device series. For MAI deposition rates in the range of 1.1–1.5 Å/s, for each rate we prepared 2 batches of 3 substrates with 4 pixels each; hence, the statistics is based on 24 pixels. For the rest of the materials, we prepared a single batch of 3 substrates for each rate (with 4 pixels each), hence the statistics is based on 12 pixels. Parameters are extracted from  $J$ – $V$  scans in forward bias.

which is dictated by the crystalline orientation with respect to the substrate. In halide perovskites prepared both by solution- and vacuum-processing, it is common to observe a preferential orientation along the [100] direction, with the most intense diffraction peaks around  $2\theta = 14^\circ$  and  $2\theta = 28.5^\circ$  (corresponding to the (100) and (200) planes). Here, this behavior holds until a MAI rate of 1.3 Å/s. Nevertheless, for higher MAI deposition rates, the intensity of the (110) and (210) peaks, located around  $2\theta = 19.9^\circ$  and  $2\theta = 31.5^\circ$ , respectively, rises considerably. To evaluate this, we have plotted the ratio between the intensities of these peaks and the intensity of the main (100) peak in Figure S7. The increase in the relative intensity of these reflections implies a lower degree of orientation of the perovskite with increasing MAI loading. As previously discussed in relation to the yellow phase, it is reasonable to think that the higher disorder induced by the addition of MA<sup>+</sup> affects the crystallographic orientation, although the underlying exact mechanism is not clearly understood. We note that, in general, hybrid organic–inorganic lead iodide perovskite thin films have been reported with different orientations, without a clear understanding of the factors governing it nor of the implications for their optoelectronic properties.<sup>43</sup>

The optical absorption of the films (Figure 3a, full data set in Figure S8) also confirms the formation of cubic perovskite at

room temperature upon MAI incorporation, showing high absorbance over all the visible spectrum and an absorption edge at approximately 800 nm. The exception is the perovskite film obtained with the lower MAI loading (0.7 Å/s), whose optical absorption resembles that of the as-deposited FAPbI<sub>3</sub> (Figure 1b), a consequence of the formation of a mixed  $\delta/\alpha$  phase. More insights about the composition can be obtained from the PL spectra of the family of materials (Figure 3b, full data set and spectra without normalization in Figure S9). A continuous red shift of the PL signal was observed upon increasing the MAI deposition rate. The FAMAPbI<sub>3</sub> films prepared using the lowest MAI rate (0.7 Å/s) exhibit a PL maximum at 781 nm, whereas the perovskite films prepared using the highest MAI rate (1.9 Å/s) show the PL maximum at 796 nm. These correspond to approximate bandgap energies ( $E_g$ ) of 1.59 and 1.56 eV, respectively. This finding is particularly interesting and counterintuitive at first. One could expect that increasing the MAI content would lead to a wider bandgap, as the  $E_g$  for vacuum-deposited pure MAPbI<sub>3</sub> was found to be 1.63 eV.<sup>44</sup> According to the literature, there is a bandgap difference of approximately 100 meV between FAPbI<sub>3</sub> ( $x = 0$ ) and MAPbI<sub>3</sub> ( $x = 1$ ), and a linear dependence of the bandgap on  $x$  might be expected in FA<sub>1-x</sub>MA<sub>x</sub>PbI<sub>3</sub>. Nevertheless, it must be noted that the FAPbI<sub>3</sub> and MAPbI<sub>3</sub> perovskite phases from which the aforementioned bandgap

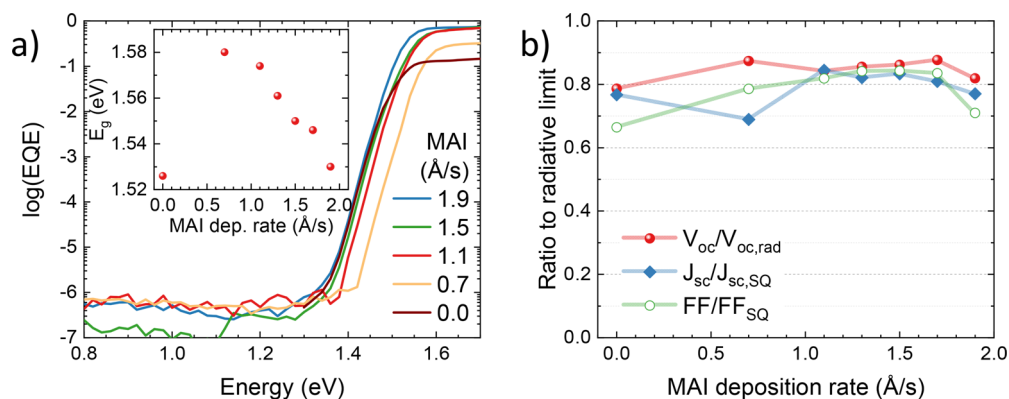


**Figure 5.** Sensitive EQE measurements and loss analysis of FAMAPbI<sub>3</sub> solar cells prepared with increasing MAI deposition rates. (a) Sensitive EQE spectra in the bandgap region (the inset shows the calculated bandgap values for each MAI rate). (b) Ratio of  $V_{oc}$ ,  $J_{sc}$ , and FF to their maximum theoretical limit for each MAI rate. The device for a MAI rate of 0 employs a FAPbI<sub>3</sub> film annealed at 150 °C.

energy difference is obtained are different crystalline phases (cubic for FAPbI<sub>3</sub> and tetragonal—distorted perovskite—for MAPbI<sub>3</sub> at room temperature). In our case, the incorporation of MAI, in the conditions in which it is performed, does not lead to a visible phase transition and the perovskite remains cubic as in pure FAPbI<sub>3</sub>. Hence, it is not surprising that the bandgap is closer to the value of pure FAPbI<sub>3</sub> even with substantial MAI incorporation. Instead, the incorporation of MAI leads to a reduction of the bandgap, which we attribute to the stabilization of the cubic  $\alpha$ -phase perovskite.

This assessment is corroborated by the PL spectra of the FAMAPbI<sub>3</sub> films obtained using the higher MAI sublimation rates (1.7 and 1.9 Å/s) which match well with that of the black  $\alpha$ -FAPbI<sub>3</sub> (Figure 1b).<sup>16</sup> Our interpretation of the structural data for the different FAMAPbI<sub>3</sub> films discussed previously is also in accordance with this assumption. The calculated MAI content was found to not directly correlate with the deposition rate used but rather to influence the stabilization of the perovskite phase and its orientation. We also noted an evolution of the morphology of the FAMAPbI<sub>3</sub> films prepared with increasing MAI deposition rates, as observed by SEM (Figure 3c). When compared with the morphology of the sublimed FAPbI<sub>3</sub>, obtained by the co-sublimation of FAI and PbI<sub>2</sub> and subsequent annealing, the incorporation of MAI induces the formation of smaller grains. The FAMAPbI<sub>3</sub> films prepared with low MAI rates have a rather heterogeneous grain distribution, yet the films prepared with MAI rates  $\geq 1.5$  Å/s have a very compact and homogeneous surface.

In view of the interesting structural, morphological, and optical properties, the whole series of perovskite films was tested in planar p-i-n perovskite solar cells with the same structure as described before. The solar cell characterization is summarized in Figure 4 and Table S1 (full data set in Figure S10).

The EQE spectra (Figure 4a) for all devices were found to be rather similar, with high photon-to-electron conversion efficiency above 0.8 throughout the visible spectrum and close to 0.9 in the red region. The origin of the lower spectral response at high energy is not clear yet, but it might originate from reflection losses or from unbalanced electron and hole mobility in the perovskite. An exception can be observed for the solar cells employing FAMAPbI<sub>3</sub> obtained with 0.7 Å/s MAI rate, which agrees with the lower optical absorption of the corresponding thin films (Figure 3a) and is attributed to the dominant yellow phase as observed by XRD. The current

density obtained from the integration of the EQE over the AM1.5 spectrum matches well with the short-circuit currents obtained from the  $J$ - $V$  curves under 1 sun illumination (Figure 4b). The  $J_{sc}$  was found to be rather constant at approximately 22 mA cm<sup>-2</sup>. Only the solar cells based on the perovskites obtained at the lowest MAI sublimation rate (0.7 Å/s) showed a reduced  $J_{sc}$  of 17 mA cm<sup>-2</sup> on average (Figure 2c, see Table S1 for record values for each perovskite formulation). The latter is the result of the lower spectral response highlighted before. The FF measured for the solar cells was found to vary between 60% and 75%, with a plateau at approximately 75% for the cells based on the perovskites obtained with MAI deposition rates in the range of 1.1–1.7 Å/s. For these solar cells, we also found the largest photovoltage: as a result, the corresponding PCEs ranged between 17.9% and 18.8%. The highest PCE was obtained for the cells using the perovskites prepared with a MAI deposition rate of 1.5 Å/s.

In order to further assess the quality of the different FAMAPbI<sub>3</sub> perovskites and the corresponding solar cells, we investigated their EQE response in the bandgap region. From the semilogarithmic plot in Figure 5a (full data set in Figure S11) one can see for all devices a steep drop of the EQE around the perovskite's bandgap. From the slope, we extracted the Urbach energies, which are in the range of 12–13 meV (see Table S2). Such low Urbach energies are an indication of a low electronic disorder that is essential to obtain high  $V_{oc}$ .<sup>45</sup> The noise level for these EQE measurements was low at  $10^{-7}$ – $10^{-6}$  and correlated with the corresponding dark currents of the devices (Figure S12). No photoresponse could be detected in the energy range of 0.8 to 1.35 eV. This implies that there are no optically active states, associated with trapped electrons/holes in the bandgap, contributing to the photocurrent. Furthermore, we extracted the bandgap of the perovskite films from these sensitive EQE measurements (inset of Figure 5a).<sup>46</sup> As discussed already for the shift of the PL signals (Figure 3b), we found a wider bandgap for low MAI rates in comparison to the annealed FAPbI<sub>3</sub> cell (without any MAI). With increasing MAI deposition rates, the FAMAPbI<sub>3</sub> perovskite bandgaps continuously decrease, reaching values close to that of the FAPbI<sub>3</sub>  $\alpha$ -phase. It is important to note that this low bandgap is reached without the need of any thermal treatments. We compared the measured key performance indicators as obtained from the  $J$ - $V$  scans with their maximal obtainable values in Figure 5b.

The radiative limit of the  $V_{oc}$ ,  $V_{oc,rad}$ , was calculated via the EQE response.<sup>47</sup> The limits for FF and  $J_{sc}$  were obtained directly from detailed balance calculations given the specific bandgap of each material (Shockley-Queisser limit, SQ).<sup>48,49</sup> It is clear that varying the MAI rate affects mostly the FF and  $J_{sc}$  ratios, whereas the  $V_{oc}$  was found to be rather constant. This suggests that the principal effect of MAI addition is the stabilization of the cubic phase, while it does not affect the recombination. Variation of the FF, however, is observed mainly for nonoptimal composition, where also the current density or the photovoltage are simultaneously reduced. In the optimum MAI rate range of 1.1–1.7 Å/s, all device parameters were found to be approximately at 80–85% of the theoretical maxima, highlighting the high quality of the perovskite films and devices reported here. At the same time, these data suggest that there is not a single limiting parameter and that all should be improved to further enhance the PCE.

Finally, we evaluated the stability of solar cells based on FAMAPbI<sub>3</sub> perovskites deposited at 1.5 Å/s MAI rate. In these devices we used an ultrathin poly(triarylamine) (PTAA) layer as the HTL, because it has been used in very efficient and stable perovskite solar cells and in view of recent reports on the instability related with the use of MoO<sub>3</sub>.<sup>50,51</sup> The devices were encapsulated with a UV-curable resin and a glass slide, and the stability was evaluated in a nitrogen atmosphere to minimize influences of extrinsic environmental factors on the degradation. Both the shelf life (in the dark) and the operational stability were evaluated. For the shelf life stability tests, the solar cells were maintained at 65 °C (using a hot plate) in the dark. Periodically, the  $J$ – $V$  characteristics under simulated 1 sun illumination were recorded at room temperature (Figure 6a).

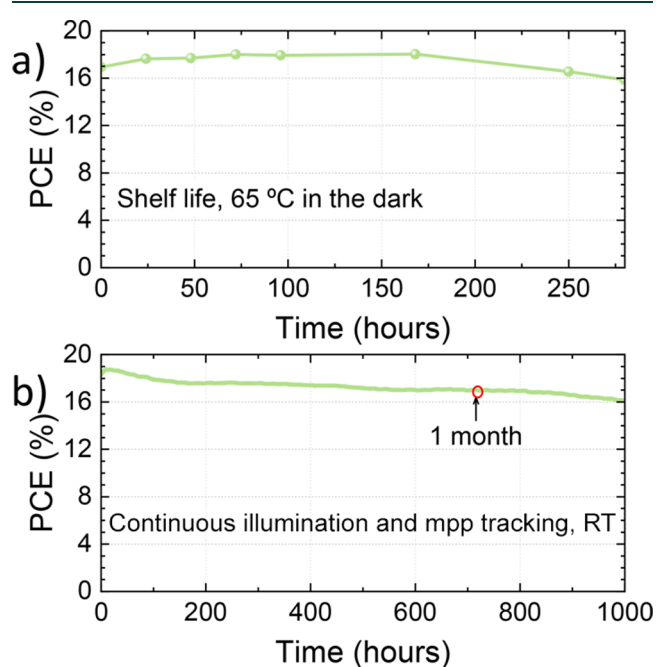


**Figure 6.** Stability assessment of encapsulated perovskite solar cells using FAMAPbI<sub>3</sub> films obtained with MAI deposition rate of 1.5 Å/s. (a) Shelf life measurements during thermal stress for devices kept in the dark at 65 °C. (b) Maximum power point tracking under continuous illumination at RT.

After 250 h of continuous thermal stress, the PCE maintained 90% of the initial value, demonstrating the thermal stability of the cubic FAMAPbI<sub>3</sub> perovskite films and of the device structure. We observed an initial increase in efficiency, which might suggest that annealing could even be beneficial for the perovskite absorber. However, annealing at the same temperature an as-prepared film does result in a degradation of corresponding the device performance (Figure S13). Most likely the rise in efficiency is device-related, as observed previously in similar p-i-n perovskite solar cells.<sup>52,53</sup> To evaluate the operational stability, the devices were maintained at their maximum power point (MPP) under simulated 1 sun equivalent illumination with white LEDs at RT (25 °C) in dry nitrogen. Under these operational conditions the solar cell exhibited a remarkable stability, maintaining 90% of the initial PCE after 1 month (720 h) of continuous operation. These findings challenge the widespread assumption that methylammonium would undermine the stability of the perovskite solar cells.

In summary, high-quality, phase-pure cubic FA<sub>1-x</sub>MA<sub>x</sub>PbI<sub>3</sub> perovskite films can be obtained using a dry sublimation process and without the need of any thermal treatment. We found that the MA<sup>+</sup> content in the perovskite film is rather insensitive to the MAI deposition rate used during cosublimation, within the range investigated herein. Independent of the MAI deposition rate, cubic perovskite films are always obtained, without any post treatment. We did observe a difference in the perovskite structural disorder and crystal orientation, although with no dramatic influence to the optoelectronic properties of the materials. The optimized perovskite formulations lead to solar cells with photovoltaic parameters at 80% of their maximum theoretical limits, highlighting the high quality of the as-deposited perovskite semiconductors. We obtained solar cells with PCE up to 18.8% that retain 90% of their initial efficiency after more than 1 month of continuous operation and also upon prolonged storage at elevated temperatures (>250 h at 65 °C).

## ■ ASSOCIATED CONTENT

### Supporting Information

The Supporting Information is available free of charge at <https://pubs.acs.org/doi/10.1021/acsenerylett.0c01473>.

Experimental methods, details of XRD analysis for all compounds, PV characterization of pure FAPbI<sub>3</sub> solar cells, quantitative determination of film composition from QCMs readings, non-normalized PL spectra, dark  $J$ – $V$  curves, tables with PV parameters, bandgaps and Urbach energies,  $J$ – $V$  curves under illumination for a solar cell with annealed perovskite film (PDF)

## ■ AUTHOR INFORMATION

### Corresponding Author

Michele Sessolo – Instituto de Ciencia Molecular, Universidad de Valencia, 46980 Paterna, Spain; [orcid.org/0000-0002-9189-3005](https://orcid.org/0000-0002-9189-3005); Email: [michele.sessolo@uv.es](mailto:michele.sessolo@uv.es)

### Authors

Lidón Gil-Escrig – Instituto de Ciencia Molecular, Universidad de Valencia, 46980 Paterna, Spain

Chris Dreessen – Instituto de Ciencia Molecular, Universidad de Valencia, 46980 Paterna, Spain; [orcid.org/0000-0001-7444-6900](https://orcid.org/0000-0001-7444-6900)

Ismail Cihan Kaya – Instituto de Ciencia Molecular, Universidad de Valencia, 46980 Paterna, Spain; Department of Metallurgical and Materials Engineering, Konya Technical University, Konya, Turkey; [orcid.org/0000-0003-0773-0391](https://orcid.org/0000-0003-0773-0391)

Beom-Soo Kim – Instituto de Ciencia Molecular, Universidad de Valencia, 46980 Paterna, Spain

Francisco Palazon – Instituto de Ciencia Molecular, Universidad de Valencia, 46980 Paterna, Spain; [orcid.org/0000-0002-1503-5965](https://orcid.org/0000-0002-1503-5965)

Henk J. Bolink – Instituto de Ciencia Molecular, Universidad de Valencia, 46980 Paterna, Spain; [orcid.org/0000-0001-9784-6253](https://orcid.org/0000-0001-9784-6253)

Complete contact information is available at:  
<https://pubs.acs.org/10.1021/acsenerylett.0c01473>

## Notes

The authors declare no competing financial interest.

## ACKNOWLEDGMENTS

The research leading to these results has received funding from the European Research Council (ERC) under the European Union's Horizon 2020 research and innovation programme Grant Agreement No. 834431 and under Grant Agreement No. 763977 of the PERTPV project, the Spanish Ministry of Science, Innovation and Universities (MICIU, MAT2017-88821-R, RTI2018-095362-A-I00, PCI2019-111829-2, EQC2018-004888-P and EQC2018-004888-P) and the Comunitat Valenciana (IDIFEDER/2018/061, EQC2018-004888-P). I.C.K. thanks TUBITAK 2214-A - International Doctoral Research Fellowship Programme for supporting his research at ICMol. C.D. acknowledges that the project that gave rise to these results received the support of a fellowship from "la Caixa" Foundation (ID 100010434, code LCF/BQ/DI19/11730020). M.S. and F.P. acknowledge the MICIU for their RyC and JdC contracts, respectively.

## REFERENCES

- (1) Jung, E. H.; Jeon, N. J.; Park, E. Y.; Moon, C. S.; Shin, T. J.; Yang, T.-Y.; Noh, J. H.; Seo, J. Efficient, Stable and Scalable Perovskite Solar Cells Using Poly(3-Hexylthiophene). *Nature* **2019**, *567* (7749), 511–515.
- (2) Jiang, Q.; Zhao, Y.; Zhang, X.; Yang, X.; Chen, Y.; Chu, Z.; Ye, Q.; Li, X.; Yin, Z.; You, J. Surface Passivation of Perovskite Film for Efficient Solar Cells. *Nat. Photonics* **2019**, *13* (7), 460–466.
- (3) Green, M. A.; Dunlop, E. D.; Hohl-Ebinger, J.; Yoshita, M.; Kopidakis, N.; Ho-Baillie, A. W. Y. Solar Cell Efficiency Tables (Version 55). *Prog. Photovoltaics* **2020**, *28* (1), 3–15.
- (4) Li, N.; Tao, S.; Chen, Y.; Niu, X.; Onwudianti, C. K.; Hu, C.; Qiu, Z.; Xu, Z.; Zheng, G.; Wang, L.; et al. Cation and Anion Immobilization through Chemical Bonding Enhancement with Fluorides for Stable Halide Perovskite Solar Cells. *Nat. Energy* **2019**, *4* (5), 408–415.
- (5) Gao, X.-X.; Luo, W.; Zhang, Y.; Hu, R.; Zhang, B.; Züttel, A.; Feng, Y.; Nazeeruddin, M. K. Stable and High-Efficiency Methylammonium-Free Perovskite Solar Cells. *Adv. Mater.* **2020**, *32* (9), 1905502.
- (6) Kim, M.; Kim, G.-H.; Lee, T. K.; Choi, I. W.; Choi, H. W.; Jo, Y.; Yoon, Y. J.; Kim, J. W.; Lee, J.; Huh, D.; et al. Methylammonium Chloride Induces Intermediate Phase Stabilization for Efficient Perovskite Solar Cells. *Joule* **2019**, *3* (9), 2179–2192.
- (7) Shockley, W.; Queisser, H. J. Detailed Balance Limit of Efficiency of P-n Junction Solar Cells. *J. Appl. Phys.* **1961**, *32* (3), 510–519.

(8) Lee, J.-W.; Kim, D.-H.; Kim, H.-S.; Seo, S.-W.; Cho, S. M.; Park, N.-G. Formamidinium and Cesium Hybridization for Photo- and Moisture-Stable Perovskite Solar Cell. *Adv. Energy Mater.* **2015**, *5* (20), 1501310.

(9) Conings, B.; Drijkoningen, J.; Gauquelin, N.; Babayigit, A.; D'Haen, J.; D'Olieslaeger, L.; Ethirajan, A.; Verbeeck, J.; Manca, J.; Mosconi, E.; et al. Intrinsic Thermal Instability of Methylammonium Lead Trihalide Perovskite. *Adv. Energy Mater.* **2015**, *5* (15), 1500477.

(10) Yang, W. S.; Park, B.-W.; Jung, E. H.; Jeon, N. J.; Kim, Y. C.; Lee, D. U.; Shin, S. S.; Seo, J.; Kim, E. K.; Noh, J. H.; et al. Iodide Management in Formamidinium-Lead-Halide-Based Perovskite Layers for Efficient Solar Cells. *Science (Washington, DC, U. S.)* **2017**, *356* (6345), 1376–1379.

(11) Turren-Cruz, S.-H.; Hagfeldt, A.; Saliba, M. Methylammonium-Free, High-Performance, and Stable Perovskite Solar Cells on a Planar Architecture. *Science (Washington, DC, U. S.)* **2018**, *362* (6413), 449–453.

(12) Saliba, M.; Matsui, T.; Domanski, K.; Seo, J.-Y.; Ummadisingu, A.; Zakeeruddin, S. M.; Correa-Baena, J.-P.; Tress, W. R.; Abate, A.; Hagfeldt, A.; et al. Incorporation of Rubidium Cations into Perovskite Solar Cells Improves Photovoltaic Performance. *Science (Washington, DC, U. S.)* **2016**, *354* (6309), 206–209.

(13) Yang, W. S.; Noh, J. H.; Jeon, N. J.; Kim, Y. C.; Ryu, S.; Seo, J.; Seok, S. I. High-Performance Photovoltaic Perovskite Layers Fabricated through Intramolecular Exchange. *Science (Washington, DC, U. S.)* **2015**, *348* (6240), 1234–1237.

(14) Pellet, N.; Gao, P.; Gregori, G.; Yang, T.-Y.; Nazeeruddin, M. K.; Maier, J.; Grätzel, M. Mixed-Organic-Cation Perovskite Photovoltaics for Enhanced Solar-Light Harvesting. *Angew. Chem., Int. Ed.* **2014**, *53* (12), 3151–3157.

(15) Zhang, Y.; Grancini, G.; Feng, Y.; Asiri, A. M.; Nazeeruddin, M. K. Optimization of Stable Quasi-Cubic FAPbI<sub>3</sub> Perovskite Structure for Solar Cells with Efficiency beyond 20%. *ACS Energy Lett.* **2017**, *2* (4), 802–806.

(16) Binek, A.; Hanusch, F. C.; Docampo, P.; Bein, T. Stabilization of the Trigonal High-Temperature Phase of Formamidinium Lead Iodide. *J. Phys. Chem. Lett.* **2015**, *6*, 1249–1253.

(17) Jodłowski, A. D.; Roldán-Carmona, C.; Grancini, G.; Salado, M.; Ralaifarisoa, M.; Ahmad, S.; Koch, N.; Camacho, L.; de Miguel, G.; Nazeeruddin, M. K. Large Guanidinium Cation Mixed with Methylammonium in Lead Iodide Perovskites for 19% Efficient Solar Cells. *Nat. Energy* **2017**, *2* (12), 972–979.

(18) Saliba, M.; Matsui, T.; Seo, J.-Y.; Domanski, K.; Correa-Baena, J.-P.; Nazeeruddin, M. K.; Zakeeruddin, S. M.; Tress, W.; Abate, A.; Hagfeldt, A.; et al. Cesium-Containing Triple Cation Perovskite Solar Cells: Improved Stability, Reproducibility and High Efficiency. *Energy Environ. Sci.* **2016**, *9*, 1989–1997.

(19) Min, H.; Kim, M.; Lee, S.-U.; Kim, H.; Kim, G.; Choi, K.; Lee, J. H.; Seok, S. I. Efficient, Stable Solar Cells by Using Inherent Bandgap of  $\alpha$ -Phase Formamidinium Lead Iodide. *Science (Washington, DC, U. S.)* **2019**, *366* (6466), 749–753.

(20) Zheng, X.; Hou, Y.; Bao, C.; Yin, J.; Yuan, F.; Huang, Z.; Song, K.; Liu, J.; Troughton, J.; Gasparini, N.; et al. Managing Grains and Interfaces via Ligand Anchoring Enables 22.3%-Efficiency Inverted Perovskite Solar Cells. *Nat. Energy* **2020**, *5* (2), 131–140.

(21) Liu, M.; Johnston, M. B.; Snaith, H. J. Efficient Planar Heterojunction Perovskite Solar Cells by Vapour Deposition. *Nature* **2013**, *501* (7467), 395–398.

(22) Malinkiewicz, O.; Yella, A.; Lee, Y. H.; Espallargas, G. M.; Graetzel, M.; Nazeeruddin, M. K.; Bolink, H. J. Perovskite Solar Cells Employing Organic Charge-Transport Layers. *Nat. Photonics* **2014**, *8* (2), 128–132.

(23) Momblona, C.; Gil-Escrig, L.; Bandiello, E.; Hutter, E. M.; Sessolo, M.; Lederer, K.; Blochwitz-Nimoth, J.; Bolink, H. J. Efficient Vacuum Deposited P-i-n and n-i-p Perovskite Solar Cells Employing Doped Charge Transport Layers. *Energy Environ. Sci.* **2016**, *9* (11), 3456–3463.

(24) Al-Ashouri, A.; Magomedov, A.; Roß, M.; Jošt, M.; Talaikis, M.; Chistiakova, G.; Bertram, T.; Márquez, J. A.; Köhnen, E.;

Kasparavičius, E.; et al. Conformal Monolayer Contacts with Lossless Interfaces for Perovskite Single Junction and Monolithic Tandem Solar Cells. *Energy Environ. Sci.* **2019**, *12* (11), 3356–3369.

(25) Lin, Q.; Armin, A.; Nagiri, R. C. R.; Burn, P. L.; Meredith, P. Electro-Optics of Perovskite Solar Cells. *Nat. Photonics* **2015**, *9* (2), 106–112.

(26) Hsiao, S.-Y.; Lin, H.-L.; Lee, W.-H.; Tsai, W.-L.; Chiang, K.-M.; Liao, W.-Y.; Ren-Wu, C.-Z.; Chen, C.-Y.; Lin, H.-W. Efficient All-Vacuum Deposited Perovskite Solar Cells by Controlling Reagent Partial Pressure in High Vacuum. *Adv. Mater.* **2016**, *28* (32), 7013–7019.

(27) Li, J.; Wang, H.; Chin, X. Y.; Dewi, H. A.; Vergeer, K.; Goh, T. W.; Lim, J. W. M.; Lew, J. H.; Loh, K. P.; Soci, C.; et al. Highly Efficient Thermally Co-Evaporated Perovskite Solar Cells and Mini-Modules. *Joule* **2020**, *4* (5), 1035–1053.

(28) Gil-Escrig, L.; Momblona, C.; La-Placa, M.-G.; Boix, P. P.; Sessolo, M.; Bolink, H. J. Vacuum Deposited Triple-Cation Mixed-Halide Perovskite Solar Cells. *Adv. Energy Mater.* **2018**, *8* (14), 1703506.

(29) Ji, R.; Zhang, Z.; Cho, C.; An, Q.; Paulus, F.; Kroll, M.; Löffler, M.; Nehm, F.; Rellinghaus, B.; Leo, K.; et al. Thermally Evaporated Methylammonium-Free Perovskite Solar Cells. *J. Mater. Chem. C* **2020**, *8* (23), 7725–7733.

(30) Borchert, J.; Milot, R. L.; Patel, J. B.; Davies, C. L.; Wright, A. D.; Martínez Maestro, L.; Snaith, H. J.; Herz, L. M.; Johnston, M. B. Large-Area, Highly Uniform Evaporated Formamidinium Lead Triiodide Thin Films for Solar Cells. *ACS Energy Lett.* **2017**, *2* (12), 2799–2804.

(31) Chiang, Y.-H.; Anaya, M.; Stranks, S. D. Multi-Source Vacuum Deposition of Methylammonium-Free Perovskite Solar Cells. *ACS Energy Lett.* **2020**, *5*, 2498.

(32) Yang, D.; Yang, R.; Priya, S.; Liu, S. Recent Advances in Flexible Perovskite Solar Cells: Fabrication and Applications. *Angew. Chem., Int. Ed.* **2019**, *58* (14), 4466–4483.

(33) Weber, O. J.; Ghosh, D.; Gaines, S.; Henry, P. F.; Walker, A. B.; Islam, M. S.; Weller, M. T. Phase Behavior and Polymorphism of Formamidinium Lead Iodide. *Chem. Mater.* **2018**, *30* (11), 3768–3778.

(34) Prathapani, S.; Choudhary, D.; Mallick, S.; Bhargava, P.; Yella, A. Experimental Evaluation of Room Temperature Crystallization and Phase Evolution of Hybrid Perovskite Materials. *CrystEngComm* **2017**, *19* (27), 3834–3843.

(35) Ma, F.; Li, J.; Li, W.; Lin, N.; Wang, L.; Qiao, J. Stable  $\alpha/\delta$  Phase Junction of Formamidinium Lead Iodide Perovskites for Enhanced near-Infrared Emission. *Chem. Sci.* **2017**, *8* (1), 800–805.

(36) Xu, Z.; Liu, Z.; Li, N.; Tang, G.; Zheng, G.; Zhu, C.; Chen, Y.; Wang, L.; Huang, Y.; Li, L.; et al. A Thermodynamically Favored Crystal Orientation in Mixed Formamidinium/Methylammonium Perovskite for Efficient Solar Cells. *Adv. Mater.* **2019**, *31* (24), 1900390.

(37) Jeon, N. J.; Noh, J. H.; Yang, W. S.; Kim, Y. C.; Ryu, S.; Seo, J.; Seok, S. I. Compositional Engineering of Perovskite Materials for High-Performance Solar Cells. *Nature* **2015**, *517* (7535), 476–480.

(38) Weber, O. J.; Charles, B.; Weller, M. T. Phase Behaviour and Composition in the Formamidinium-Methylammonium Hybrid Lead Iodide Perovskite Solid Solution. *J. Mater. Chem. A* **2016**, *4* (40), 15375–15382.

(39) Weller, M. T.; Weber, O. J.; Frost, J. M.; Walsh, A. Cubic Perovskite Structure of Black Formamidinium Lead Iodide,  $\alpha$ -[HC(NH<sub>2</sub>)<sub>2</sub>]PbI<sub>3</sub>, at 298 K. *J. Phys. Chem. Lett.* **2015**, *6* (16), 3209–3212.

(40) Savikhin, V.; Jagadamma, L. K.; Purvis, L. J.; Robertson, I.; Oosterhout, S. D.; Douglas, C. J.; Samuel, I. D. W.; Toney, M. F. Morphological, Chemical, and Electronic Changes of the Conjugated Polymer PTB7 with Thermal Annealing. *iScience* **2018**, *2*, 182–192.

(41) Lohmann, K. B.; Patel, J. B.; Rothmann, M. U.; Xia, C. Q.; Oliver, R. D. J.; Herz, L. M.; Snaith, H. J.; Johnston, M. B. Control over Crystal Size in Vapor Deposited Metal-Halide Perovskite Films. *ACS Energy Lett.* **2020**, *5* (3), 710–717.

(42) Kim, B.-S.; Gil-Escrig, L.; Sessolo, M.; Bolink, H. J. Deposition Kinetics and Compositional Control of Vacuum-Processed CH<sub>3</sub>NH<sub>3</sub>PbI<sub>3</sub> Perovskite. *J. Phys. Chem. Lett.* **2020**, *11*, 6852–6859.

(43) Lohmann, K. B.; Patel, J. B.; Rothmann, M. U.; Xia, C. Q.; Oliver, R. D. J.; Herz, L. M.; Snaith, H. J.; Johnston, M. B. Control over Crystal Size in Vapor Deposited Metal-Halide Perovskite Films. *ACS Energy Lett.* **2020**, *5* (3), 710–717.

(44) Palazon, F.; Pérez-Del-Rey, D.; Dănekamp, B.; Dreessen, C.; Sessolo, M.; Boix, P. P.; Bolink, H. J. Room-Temperature Cubic Phase Crystallization and High Stability of Vacuum-Deposited Methylammonium Lead Triiodide Thin Films for High-Efficiency Solar Cells. *Adv. Mater.* **2019**, *31* (39), 1902692.

(45) Chantana, J.; Kawano, Y.; Nishimura, T.; Mavlonov, A.; Minemoto, T. Impact of Urbach Energy on Open-Circuit Voltage Deficit of Thin-Film Solar Cells. *Sol. Energy Mater. Sol. Cells* **2020**, *210* (January), 110502.

(46) Rau, U.; Blank, B.; Müller, T. C. M.; Kirchartz, T. Efficiency Potential of Photovoltaic Materials and Devices Unveiled by Detailed-Balance Analysis. *Phys. Rev. Appl.* **2017**, *7* (4), 44016.

(47) Rau, U. Reciprocity Relation between Photovoltaic Quantum Efficiency and Electroluminescent Emission of Solar Cells. *Phys. Rev. B: Condens. Matter Mater. Phys.* **2007**, *76* (8), 85303.

(48) Shockley, W.; Queisser, H. J. Detailed Balance Limit of Efficiency of P-n Junction Solar Cells. *J. Appl. Phys.* **1961**, *32* (3), 510–519.

(49) Rühle, S. Tabulated Values of the Shockley-Queisser Limit for Single Junction Solar Cells. *Sol. Energy* **2016**, *130*, 139–147.

(50) Saliba, M.; Matsui, T.; Domanski, K.; Seo, J.-Y.; Ummadisingu, A.; Zakeeruddin, S. M.; Correa-Baena, J.-P.; Tress, W. R.; Abate, A.; Hagfeldt, A.; et al. Incorporation of Rubidium Cations into Perovskite Solar Cells Improves Photovoltaic Performance. *Science (Washington, DC, U. S.)* **2016**, *354* (6309), 206–209.

(51) Schloemer, T. H.; Raiford, J. A.; Gehan, T. S.; Moot, T.; Nanayakkara, S.; Harvey, S. P.; Bramante, R. C.; Dunfield, S.; Louks, A. E.; Maughan, A. E.; et al. The Molybdenum Oxide Interface Limits the High-Temperature Operational Stability of Unencapsulated Perovskite Solar Cells. *ACS Energy Lett.* **2020**, *5* (7), 2349–2360.

(52) Momblona, C.; Gil-Escrig, L.; Bandiello, E.; Hutter, E. M.; Sessolo, M.; Lederer, K.; Blochwitz-Nimoth, J.; Bolink, H. J. Efficient Vacuum Deposited P-i-n and n-i-p Perovskite Solar Cells Employing Doped Charge Transport Layers. *Energy Environ. Sci.* **2016**, *9* (11), 3456–3463.

(53) Babaei, A.; Dreessen, C.; Sessolo, M.; Bolink, H. J. High Voltage Vacuum-Processed Perovskite Solar Cells with Organic Semiconducting Interlayers. *RSC Adv.* **2020**, *10* (11), 6640–6646.